Inorganic Chemistry

pubs.acs.org/IC

Article

Isolation of a Bridging Phosphide-Supported Redox-Active Neutral Ag_4-Nanocluster as a Molecular Energy Storage Material

Nivedya K. Vikas, Mayur Thosare, Sayed Imroz Hossain, Akshara Purushothaman, Asutosh Patra, Ashwath Kudlu, Manasi Baccha, Babasaheb R. Sankapal,* and Sudipta Roy*

Cite This: https://doi.org/10.1021/acs.inorgchem.6c02414

Read Online

ACCESS | Metrics & More | Article Recommendations | Supporting Information

ABSTRACT: Stabilization of robust and structurally well-defined Ag^I-based nanoclusters as molecular pseudocapacitors for electrochemical energy storage has been unexplored. Herein, we report on the novel synthesis, solid-state isolation, and pseudocapacitor studies of an atomically precise neutral redox-active Ag_4 nanocluster $[((Cy\text{-}cAI)P(Dipp))_4Ag_4]$ (**2**), supported by the unique bulky μ_2-phosphide ligands. Cyclic voltammetry (CV) studies on **2** revealed a possible quasi-reversible one-electron reduction, suggesting *in situ* generation of the corresponding radical anion $\mathbf{2}^{\bullet-}$, which was further supported by the electron paramagnetic resonance (EPR) spectroscopy and Mulliken spin density calculations. The unprecedented effort to fabricate an electrode by depositing **2** on a solid support, investigating the pseudocapacitive behavior in a 1 M $NaClO_4$ electrolyte by employing a three-electrode cell arrangement, was successful. The corresponding CV profiles exhibited a quasi-rectangular profile with redox peaks, signifying a combination of electric double-layer capacitive (EDLC) and pseudocapacitive effects with the highest specific capacitance value of 168.9 F g^{-1} (185.8 mF cm^{-2}) at a 2 mV s^{-1} scan rate.

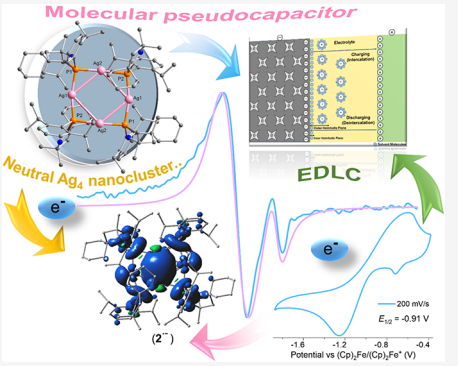

INTRODUCTION

The significantly increased fossil fuel depletion and environmental pollution demand efficient methods to develop low-cost and renewable energy storage devices. Pseudocapacitors have potential advantages of high-power density, rapid charge−discharge capability, and long cycle life depending on the design of the electrodes, which can support fast and reversible interfacial or redox processes, potentially solving the problems of energy crisis and environmental concerns.[1−3] As a result, such materials can bridge the power-energy gap between conventional dielectric capacitors and rechargeable batteries, and therefore, have emerged as exciting energy storage devices for next-generation electronics, electric vehicles, and grid-level buffering.[4−6] Various metal oxides, such as RuO_2, MnO_2, etc.,[7−9] and conducting organic polymers have been known to exhibit faradic pseudocapacitance.[10,11] However, incorporation of metal nanoparticles into the conducting polymers can significantly improve the electrical conductivity of the conjugated polymers, where the size of the nanoparticles plays a crucial role. Among the numerous metals, Ag nanoparticles have attracted widespread attention due to their higher electrical conductivity and chemical stability.[12−14] For example, Zhang et al. reported carbonized wood fibers, composited with Ag nanoparticles, which exhibited the specific capacitance of 250 F·g^{-1} at 1 A·g^{-1}.[15] While nanocomposites in combination with conventional organic polymers have several advantages as active electrode materials in supercapacitor studies, organic radical compounds suffer from poor electrical conductivity and dissolution in low molecular weight organic electrolytes.[16] To solve such issues, various redox-active metal complexes have recently attracted considerable attention to design potential supercapacitors due to their tunable structures, well-defined electronic states, and possibility of tailoring charge transport and ion accessibility at the nanoscale.[17,18] Designing multinuclear transition-metal-based molecular clusters, introducing various stabilizing ligands, has gained significant attention due to their unique electronic states, which arise from the intermetallic interactions and distinguish them from their respective mononuclear counterparts.[19] In this regard, coinage metals (Cu, Ag, and Au) are noteworthy, affording multinuclear clusters with noncovalent intermetallic interactions.[20] However, synthesis of Ag NCs[21] is more challenging due to their relative susceptibility in solution under atmospheric conditions. So far, polyoxometalates, thiacalix[4]arenes, and related ligand systems have been utilized to gain precise control over the size, shape, and composition of Ag NCs.[22] Owing to the discrete electronic

Received: May 12, 2026
Revised: June 23, 2026
Accepted: June 29, 2026

Scheme 1. (a) Stabilization of Neutral Ag_4 Nanocluster $[(((Cy\text{-}cAI)P(Dipp))_4Ag_4]$ (2) by Bulky Phosphide Ligand[a]

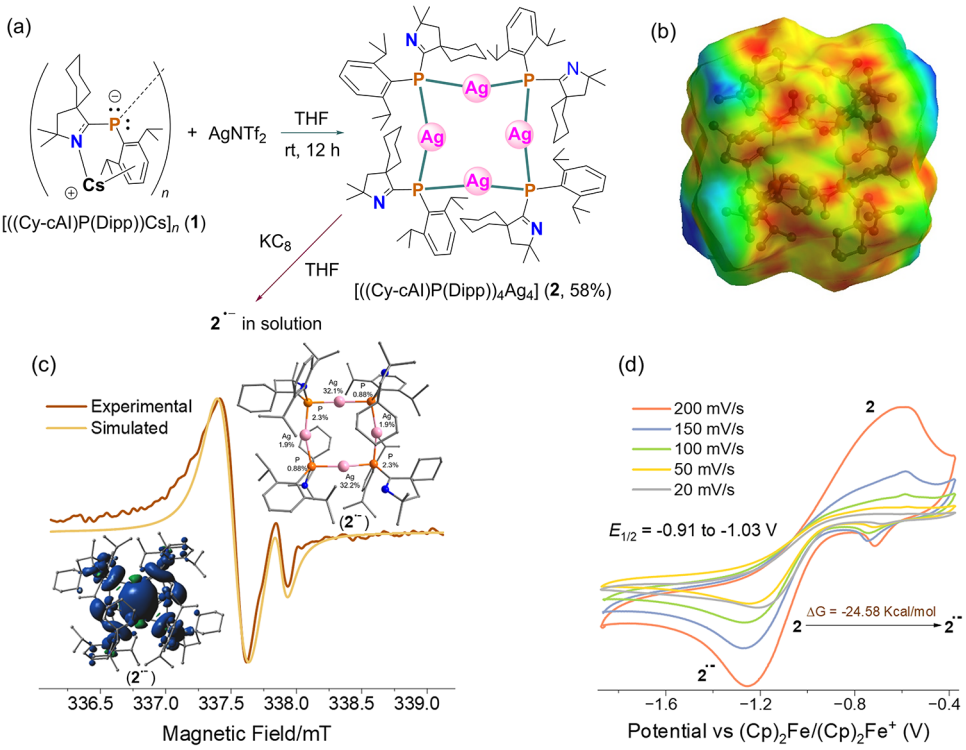

[a](b) Molecular electrostatic potential plot of **2** (red to blue: electron-rich (red) to electron-deficient regions (blue)). (c) X-band EPR spectra of THF solution containing 1:1 molar ratio of **2** + KC_8 at 298 K. Maroon and yellow lines represent the experimental and simulated spectra, respectively. Simulation has been performed using the EasySpin program.[32] *Inset*: Mulliken spin density plot of $\mathbf{2}^{\bullet-}$ in doublet spin ground state, calculated at B3LYP-D3(BJ)/def2-TZVP level of theory.[33] (d) Cyclic voltammograms of **2** at scan rates of 20, 50, 100, and 150, 200 mV s^{-1} in THF at 298 K, using 0.1 M $[n\text{-}Bu_4N][PF_6]$ as supporting electrolyte with a glassy carbon working electrode (WE), platinum wire counter electrode (CE), and Ag wire reference electrode (RE). The voltammograms have been referenced to the internal standard $(Cp)_2Fe/(Cp)_2Fe^+$, which was added after the measurements.

structures and pronounced quantum confinement effects, Ag NCs may exhibit tunable photophysical properties, including near-infrared (NIR) emission,[23−25] which has attracted considerable attention for applications in bioimaging and optoelectronic devices due to enhanced tissue penetration. Furthermore, chiral and circularly polarized luminescent (CPL) Ag NCs have emerged as promising materials for advanced technologies, such as information storage, encrypted communication, and security encoding. For example, Sun and co-workers reported a supramolecular assembly comprising a luminescent Ag_6 NC and γ-cyclodextrin that exhibits CPL activity by synergistically combining the properties of both components.[26] Beyond luminescence, Ag NCs have demonstrated remarkable nonlinear optical responses, which can be tailored through kernel alloying with various metals, such as Ag, Au, Pt, and Pd, into a metal−ligand cluster template.[27] Moreover, the use of bialkynyl ligands enabled the isolation of the chiral nanoclusters *R/S*-Ag_{39} and *R/S*-Ag_{40}, resulting in a notable red shift of NIR-phosphorescence from 1088 to 1150 nm.[28] In addition to their structural diversity, Ag NCs have found applications in chemical sensing. For example, Morsali and co-workers reported a ferrocene-functionalized tetranuclear Ag cluster that was employed in the fabrication of FcAgCs/ITO thin-film electrodes for the sensitive detection of H_2O_2.[29] Suturina and co-workers described an unusual emissive Ag cluster featuring a Ag-centered, phosphorus-capped tetrahedral $[Ag@Ag_4(\mu_3\text{-}P)_4]$ unit encapsulated within an N_{12} icosahedral framework, highlighting the structural versatility and intriguing photophysical properties of Ag-based cluster systems.[30] However, the application of structurally well-defined bulky phosphide-supported molecular Ag NCs as molecular pseudocapacitors is rarely explored.

Herein, we depict the stabilization, synthesis, solid-state isolation, and detailed characterization of a structurally well-defined soluble, tetranuclear silver NC $[(((Cy\text{-}cAI)P(Dipp))_4Ag_4]$ (**2**), with a planar $Ag(I)_4$ core, supported by a novel monoanionic group 15-based bulky phosphide ligand by treating highly reactive linear polymer of the Cs-(imino)-phosphide complex[31] with $AgNTf_2$ under an argon atmosphere. Detailed spectroscopic, thermal, and surface analyses along with quantum chemical calculations have been performed to gain deeper insights into the nature of its structure and electronic properties. Moreover, the possible utilization of **2** in various electrochemical experiments has been explored within a three-electrode setup, which revealed that **2** possesses intrinsic charge storage properties, suggesting its potential use as an active substance in batteries.

RESULTS AND DISCUSSION

Bright orange crystals of the polymeric Cs-complex $[(((Cy\text{-}cAI)P(Dipp))Cs]_n$ (**1**) (Cy = cyclohexyl; cAI = cyclic alkyl(imino); Dipp = 2,6-di-isopropylphenyl)[31] were treated with silver bis(trifluoromethanesulfonyl)imide ($AgNTf_2$) in a 1:1 molar ratio in anhydrous THF at room temperature (rt) for 12 h under an argon atmosphere. The resulting dark green reaction mixture was filtered and stored for crystallization upon

https://doi.org/10.1021/acs.inorgchem.6c02414
Inorg. Chem. XXXX, XXX, XXX−XXX

concentration up to 2−3 mL in a freezer at −40 °C. After 1 week, block-shaped pale-yellow crystals of the metal cluster $[((Cy\text{-}cAI)P(Dipp))_4Ag_4]$ (**2**) with $Ag(I)_4$ core were isolated in 58% yield (Scheme 1).

The purity of cluster **2** was established by elemental analyses and powder X-ray diffraction. The crystals of **2** were found to be stable for several months under an argon atmosphere, and for a few weeks under air at an ambient temperature. Cluster **2** was soluble in polar solvents, e.g., THF, acetonitrile, DCM, etc., and the solutions of **2** were stable under an argon atmosphere for several months at ambient temperature, but decomposed under air after 7 days. **2** was decomposed at 137−140 °C. Further, thermogravimetric analysis (TGA) was performed to investigate the thermal stability of **2**, where the TGA profile showed a multistep decomposition process (see the SI). **2** °C in solid-state, above which it lost almost half of its weight (52.5%) in a temperature range of 200 to 435 °C, attributed to the decomposition of the major organic ligand framework. A gradual mass loss of 20.8% was observed between 477.6 and 1000 °C, corresponding to the continued degradation of the residual framework.

At rt, ^{31}P NMR spectrum of the Ag_4 cluster **2** in THF-d_8 exhibited no detectable signal. However, upon lowering the temperature to 223 K, a broad multiplet was observed at −109.8 ppm due to coupling with neighboring two-coordinate Ag ions (^{107}Ag and ^{109}Ag nuclei), which was significantly downfield shifted compared to that of Ag_7 (−127.3 ppm),[34] and upfield shifted compared to those of Ag_8 (−87 ppm),[35] and Ag_5 (−23.3 ppm)[34] clusters, revealing electron-rich P centers. The Raman spectrum of cluster **2** exhibited distinct bands at 93 and 128 cm^{-1}, corresponding to the characteristic Ag−P stretching modes (see SI), which are comparable with the reported ν(Ag−P) symmetric stretching frequencies observed for $[(CH_3)_3P{\cdot}AgI]_4$ (122 cm^{-1}) and $[(^tBu)_3PAgP(^tBu)_3]^+$ (95 cm^{-1}).[36,37]

The electrospray ionization mass spectrometry (ESI-MS) analysis of a THF solution of **2** showed a peak at m/z 1896.06, corresponding to the $[((Cy\text{-}cAI)P(Dipp))_4Ag_4]$ (**2**) + CH_3CN + $(H)^+$ cation (Figure 1).

The isotropic distribution of the species closely matched the corresponding simulated spectrum. The X-ray photoelectron spectroscopy (XPS) of **2** was performed to confirm the oxidation state of the Ag ions present in the cluster. Two well-resolved bands at 368.3 and 374.2 eV, corresponding to the $3d_{5/2}$ and $3d_{3/2}$ states, respectively, were observed in the spectrum, confirming the presence of metallic Ag^I in the Ag_4 nanocluster (**2**) (see SI).

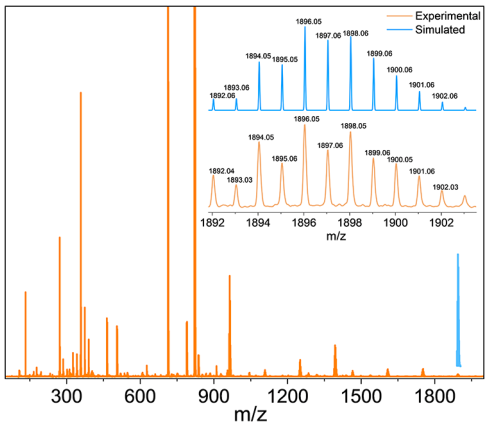

Figure 1. Experimental (orange) and simulated (blue) full-range mass spectrum of isolated crystals of $[((Cy\text{-}cAI)P(Dipp))_4Ag_4]$ (**2**) + CH_3CN + $(H)^+$ cation; $[((Cy\text{-}cAI)P(Dipp))_4Ag_4] = C_{92}H_{140}Ag_4N_4P_4$.

The electrochemical behavior of **2** was investigated by cyclic voltammetry (CV) studies of a THF solution of **2** in 0.1 M $[n\text{-}Bu_4N]PF_6$ as the electrolyte at multiple scan rates ranging from 20 to 200 mV s^{-1}, showing an electrochemical process in the voltage range from −0.4 to −1.9 V (Scheme 1d). The corresponding cyclic voltammograms revealed a quasi-reversible electron transfer process with $E_{1/2}$ ranging from −0.91 to −1.03 V, suggesting the formation of the corresponding radical anion $\mathbf{2}^{\bullet-}$ (Scheme 1d). The CV of the previously reported Ag_4 cluster having two μ_3-$C_{acetylene}$ bridges, stabilized by dppf and methanol ligands, exhibited redox peaks in the positive potential range ($E_{1/2}$ = 1.076 and 1.022 V), one corresponding to the ferrocene-centered one-electron reduction, and the other quasi-reversible peak, responsible for oxidation of dppf ligand.[29] In contrast, an irreversible reduction process was reported for the Ag_4 nanocluster stabilized by py_3p ligand in the negative potential region.[30] Further, the chemical reduction of cluster **2** was performed using KC_8 (1:1 molar ratio) in THF to investigate the feasibility of generating the radical anion $\mathbf{2}^{\bullet-}$ *in situ*. To our delight, the X-band EPR spectrum of the resulting reaction solution exhibited a broad resonance with rhombic nature, centered near ∼337 mT with a g value close to 2.0, indicating a metal-centered paramagnetic species. The presence of a single signal without resolved hyperfine splitting suggests an S = 1/2 paramagnetic species with an unpaired electron (Scheme 1c). Subsequently, we performed the XPS analysis of the dry crystalline solid obtained upon reduction of **2**, which revealed the presence of both Ag^0 and Ag^I centers (SI).

The Mulliken spin density[33] analysis of $\mathbf{2}^{\bullet-}$, calculated at the UB3LYP/def2-TZVP level of theory, showed that the majority of spin is delocalized (α-spin density) on the central Ag_4 unit (Scheme 1c; *inset*) with minor contributions from the neighboring P atoms (0.8−2.3%) (Scheme 1c, *insets*). Notably, the two Ag atoms bear the majority of the spin population (32.1% each), while the remaining two contribute negligibly (1.9% each), highlighting an uneven spin distribution within the metal core. In contrast, the β-spin density is primarily delocalized over the C and N atoms. The accumulation of spin densities between two Ag atoms could be due to the stronger Ag···Ag interaction in $\mathbf{2}^{\bullet-}$ (Scheme 1c, *inset*).

Structural characterization of the nanocluster $[((Cy\text{-}cAI)P(Dipp))_4Ag_4]$ (**2**) by single-crystal X-ray diffraction revealed that the tetranuclear Ag cluster crystallizes in the triclinic P-1 space group (Figure 2). There is a center of inversion present within this molecule. The molecular structure of **2** comprises four Ag^I ions and four monoanionic bulky phosphide ligands $[(Cy\text{-}cAI)P(Dipp)]^-$. The NC **2** has a nearly planar-rectangular Ag_4 core, where each of the four Ag^I ions is bonded to two μ-P bridging atoms of the two phosphide ligands [97.03(4), 100.83(5)°]. The Ag−Ag distances in **2** are 3.56 to 3.67 Å. Previously reported 1,1-bisdiphenylphosphinoferrocene (dppf) stabilized Ag_4 nanocluster, reported by Kuan-Guan Liu and co-workers, features a rhombus core structure with significantly shorter Ag···Ag interaction in the range from 3.05019(6) to 3.1930(7) Å.[29]

In contrast, Ag−Ag distances along the edges of the Ag_4 tetrahedron are too long [5.0031(7)−5.2553(7) Å] for Ag-

https://doi.org/10.1021/acs.inorgchem.6c02414
Inorg. Chem. XXXX, XXX, XXX−XXX

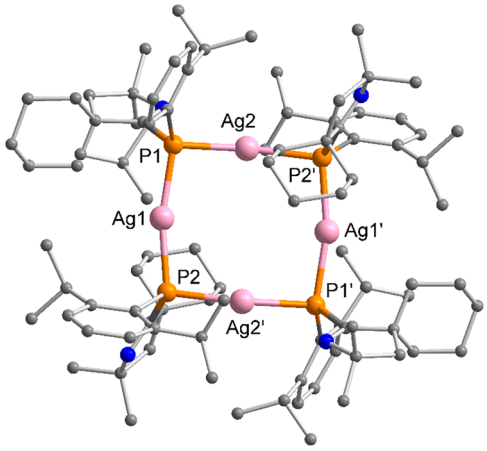

Figure 2. Molecular structure of the nanocluster [((Cy-cAI)P(Dipp))$_4$Ag$_4$] (**2**). H atoms were omitted for clarity. Color code: Ag, pink; P, orange; C, gray; N, blue. Selected experimental [calculated at B3LYP/def2-SVP] bond lengths [Å], and bond angles [°]: Ag2−P1 2.3770(12) [2.3860], Ag2−P2′ 2.3986(12) [2.4067], P1−C7 1.846(5) [1.836], N1−C7 1.259(6) [1.272], P1−Ag2−P2′ 167.83(5) [165.83], C7−P1−Ag2 112.43(15) [113.92], Ag1−P1−Ag2 97.03(4) [97.19].

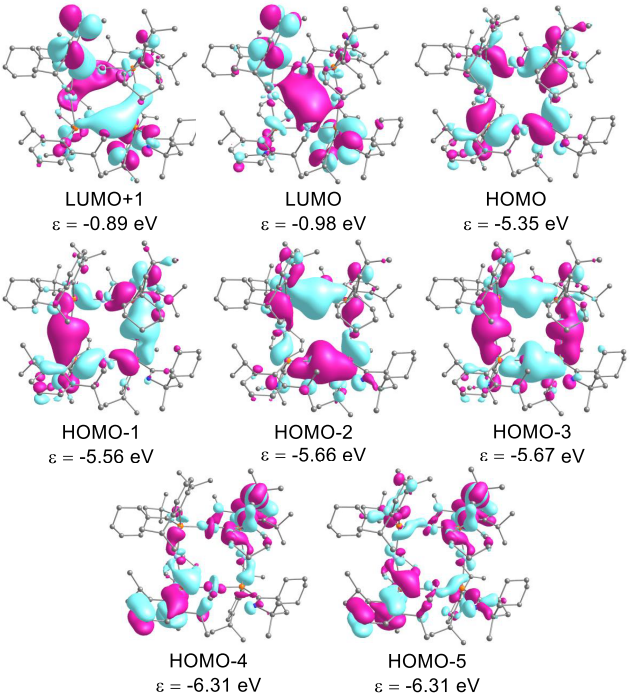

Figure 3. Representative Kohn−Sham orbitals of nanocluster [((Cy-cAI)P(Dipp))$_4$Ag$_4$] (**2**), calculated at the B3LYP-D3(BJ)/def2-TZVP level of theory.

centered phosphorus-tetracapped tetrahedron, the [Ag@Ag$_4$(μ_3-P)$_4$] core with tris(2-pyridyl)phosphine ligand (Pyy-Py$_3$P).[30] Notably, silyl- and germyl-bridged neutral square-planar Ag$_4$ have very short Ag−Ag distances (2.695 and 2.704 Å), suggesting strong argentophilic interaction.[38] The Ag−Ag distances in the Ag$_{12}$ kernel of a Ag$_{102}$ molecule reported by Sun and co-workers fall in the range of 2.748−2.847 Å.[39] The Ag−P bond distances of **2** [2.3770(12) and 2.3986(12) Å] fall within the range observed for dppf stabilized Ag$_4$ cluster [2.3769(14) to 2.3988(13) Å] indicating comparable bond length.[29] However, these values are comparatively shorter than Py$_3$P-supported Ag$_4$ clusters by [Ag−P, 2.5766(16)−2.6095(15) Å], reflecting relatively weaker Ag−P interaction in the latter system.[30] Furthermore, in comparison with other nuclearity Ag clusters stabilized by phosphorus ligands, the Ag−P bond lengths in **2** are slightly shorter than those of the previously reported Ag$_5$, Ag$_7$, Ag$_8$ and Ag$_{12}$ nanoclusters (2.39 to 2.56 Å).[32,40] However, these values are comparable to those observed in Ag$_{12}$ nanocluster bearing a different metal framework supported by cAACPK ligand (2.37 to 2.45 Å),[25] but are longer than the Ag−P distances reported for an Ag$_{10}$ nanocluster (2.23 to 2.48 Å).[32] Furthermore, the Ag−P−Ag bond angles [97.03(4), 100.83(5)°] of the central Ag$_4$ unit (**2**) are wider than those observed for the analogous Ag$_4$ core present in previously described Ag$_5$ and Ag$_7$ NCs.[40]

Geometry optimization for cluster **2** in the singlet ground state has been performed at the B3LYP-D3(BJ)/def2-TZVP[41] level of theory followed by the natural bond orbital (NBO)[42] analysis to elucidate the orbital interactions and bond polarization, which revealed that the HOMO of **2** primarily contributes to the interaction between Ag d_{xy} orbital and the π orbital of the P atom, indicating effective d_π−p_π conjugation (Figure 3). Notably, one P center simultaneously interacts with two Ag atoms, highlighting a multicenter delocalization pathway within the Ag−P framework. This result is corroborated by the 3c−2e bond with the ON of 1.85, 1.73 (see Table S6 in SI). The LUMO displays a diffuse electron density distributed over the d e-cloud of all four Ag atoms, suggesting that the unoccupied orbital manifold is largely metal-centered and may facilitate metal-based acceptor behavior. In the HOMO−1 and HOMO−2 orbitals, cooperative participation of two different Ag d orbitals is observed. The d_{xy} orbital of one Ag atom overlaps with the phosphorus π orbital from one side, while the d_{z2} orbital of another Ag atom interacts with the same π system from the opposite side. This arrangement further supports a 3c delocalized interaction involving Ag−P−Ag. The HOMO−3 orbital predominantly involves interaction between the Ag d_{z2} orbital and the phosphorus π orbital, representing a more localized d-π interaction compared to the higher-energy occupied orbitals. Overall, the NBO results demonstrate pronounced Ag(d)→P(π) donor−acceptor interactions and multicenter metal−ligand delocalization, which play a key role in stabilizing the electronic structure of cluster **2**. A partial single-bond character is observed for the Ag−P interaction, as indicated by a Wiberg bond index (WBI)[43] of 0.40 (see Table S7 in SI).

Subsequently, the HOMO−LUMO energy gap of NC **2** is calculated to be 4.37 eV, indicating a relatively large gap and thereby suggesting a high degree of electronic stability. In contrast, upon reduction to the corresponding radical anion (**2**$^{\bullet-}$), a significant decrease in the energy gap is observed, with the value dropping to 1.22 eV. This pronounced reduction reflects enhanced electronic flexibility and increased reactivity in the radical species compared to their neutral counterparts. To reliably assess the Ag−P bonding interactions, Mayer bond order (MBO)[44] calculations were performed alongside WBI analysis. The computed bond indices show that the majority of Ag−P interactions fall within the range of 0.55−0.73, indicative of predominantly single-bond character. In contrast, the Ag2−P7 and Ag3−P5 interactions exhibit comparatively lower bond order values (~0.36), suggesting weakened bonding with partial single-bond character. These deviations point toward

https://doi.org/10.1021/acs.inorgchem.6c02414
Inorg. Chem. XXXX, XXX, XXX−XXX

nonuniform metal−ligand interactions within the framework, reflecting localized variations in electronic distribution and bonding strength. The bond is notably polarized toward the P atom, reflecting the greater electron density localization on P relative to Ag. For the P−C bond involving the cAAC carbene, NBO analysis shows that the bond is also polarized toward the phosphorus center (61.3%). Similarly, in the P−C bond connecting the Dipp substituent, the electron density distribution remains biased toward phosphorus (60.1%) polarization on the P atom. These results give a clear indication that P acts as the dominant electron density acceptor in its bonding interactions with both the metal center and the adjacent carbon-based ligands. Reduction of cluster **2** by one electron affords the corresponding radical anion with a doublet ground state.

NBO analysis was performed at the UB3LYP-D3(BJ)/def2-TZVP level of theory on $\mathbf{2}^{\bullet-}$ at the doublet spin ground state to gain insight into the bonding interactions between the Ag and P atoms. The overall orbital characteristics remain largely consistent with those of neutral **2**, with the key distinction being the presence of a singly occupied molecular orbital (SOMO). This unpaired electron resides in the α-spin channel at −0.93 eV, while the corresponding β-spin orbital remains unoccupied (see SI).

The topological analysis of the electron density has been performed using the quantum theory of atoms in molecules (QTAIM),[45] which provided further insight into the nature of bonding of cluster **2** (Figure 4). The positive Laplacian values

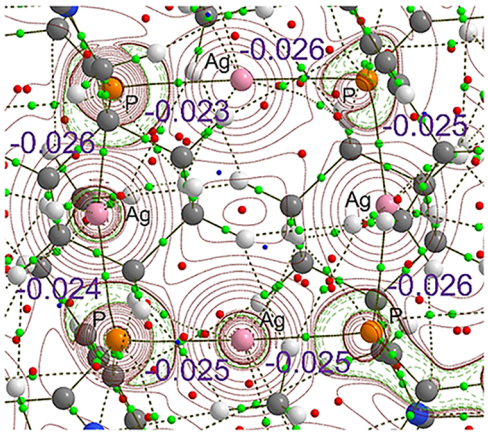

Figure 4. Contour plot of the Laplacian of electron density $[\nabla^2\rho(r)]$ for cluster **2** across the Ag−P−Ag plane, calculated at the B3LYP/def2-TZVP level of the theory. Solid maroon lines indicate areas of charge depletion ($\nabla^2\rho(r) > 0$), while dotted green lines denote charge concentration ($\nabla^2\rho(r) < 0$). Solid lines connecting atomic nuclei (gray) are the bond paths, and green spheres on the bond path indicate the bond critical points (BCPs). Energy density values at BCPs are written in purple.

($\nabla^2\rho(r) > 0$) at the bond critical points (BCPs) of the Ag−P interactions indicated a depletion of electron density in the interatomic region, reflecting the contraction of $\rho(r)$ toward the respective nuclei.

The electron density values ($\rho(r)$) in the range of 0.078−0.082, together with the positive Laplacian, gave a clear indication of closed-shell interactions. Additionally, the low ellipticity values (ε = 0.049−0.062) further supported the predominance of single-bond character of the Ag−P bonds. In contrast, the P−C bonds exhibit negative Laplacian values ($\nabla^2\rho(r) < 0$), indicative of open-shell interactions. The relatively higher ellipticity values (ε = 0.142−0.352) suggested the presence of π-character within these bonds. Notably, the P−C_{cAAC} bond displayed the highest ellipticity value, highlighting the enhanced π-contribution along this interaction. Furthermore, the negative total energy density H(r) observed for all Ag−P, P−C_{cAAC}, and P−C_{Dipp} interactions confirmed the covalent interactions.

The electron localization function (ELF)[46] calculations on **2** were performed at the B3LYP-D3(BJ)/def2-TZVP level of theory using Multiwfn program (Figure 5),[47a,b] which revealed

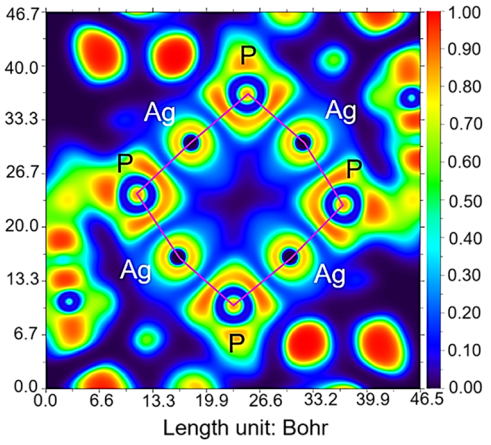

Figure 5. ELF[46] plot of **2**, calculated at the B3LYP-D3(BJ)/def2-TZVP level of theory. The color bar on the left-hand side indicates increasing localization. The core charge areas are characterized by circular fields around atoms with high (≈ 1.0) values of ELF (red), while the chemical bonds are described by irregular localization domains (cyan) with smaller values of ELF.

the involvement of di-, tri-, and hexa-synaptic basins. A disynaptic basin was observed between Ag and P atoms with a population of 1.87 e. In addition, four trisynaptic basins were identified with populations ranging from 1.91 to 2.00 e. The presence of these trisynaptic basins was consistent with NBO analysis, which indicated a 3c−2e bonding interaction, polarized predominantly toward the P atom. A hexa-synaptic basin was detected involving all four Ag atoms along with the adjacent C and H atoms of the Dipp groups, indicating extensive electron delocalization. A similar interaction pattern was also evident from the LUMO+1 orbital.

The UV−vis absorption spectrum of **2** in THF was recorded at 298 K under an argon atmosphere, which showed two absorption bands with the absorption maxima (λ_{max}) at 250 and 349 nm (see SI). The time-dependent density functional theory (TD-DFT)[48] calculations were performed on **2**, both in the gas phase and in THF solvent, at the B3LYP-D3(BJ)/def2-TZVP level of theory to assess the nature of the electronic transitions responsible for the absorption characteristics. The computed absorption maxima were found to be in good agreement with the experimentally observed values in both cases. Furthermore, the dominant excitations exhibited pronounced metal-to-ligand charge transfer (MLCT). In the gas phase, the most significant transition was attributed to the HOMO−1 → LUMO+10 excitation, occurring at 340.06 nm with an oscillator strength (f) of 0.093. Thorough analysis of the involved molecular orbitals revealed that the HOMO−1 is primarily composed of the d_{xy} orbitals of Ag atoms interacting with the P atoms, whereas the LUMO+10 was predominantly

https://doi.org/10.1021/acs.inorgchem.6c02414
Inorg. Chem. XXXX, XXX, XXX−XXX

associated with the $\pi^*_{C=N}$ antibonding orbital. Consequently, the electronic excitation corresponds to charge transfer from the Ag−P framework to the $\pi^*_{C=N}$ acceptor orbital (Figure S25 in SI). In presence of THF as the solvent, the dominant absorption band arises from the HOMO−2 → LUMO+3 transition, exhibiting a higher oscillator strength of 0.151 and a calculated absorption wavelength of 355.08 nm, which closely matches the experimentally observed value of 349.0 nm. The HOMO−2 orbital is characterized by interactions between the Ag d_{z2} orbitals and the P π orbitals, while the LUMO+3 retains substantial $\pi^*_{C=N}$ character. Similar to the gas-phase excitation, the transition in solution was found to be dominated by MLCT from the Ag−P framework to the ligand-centered $\pi^*_{C=N}$ orbital (Figure S26 in SI).

NC **2** exhibited a prominent emission maximum (λ_{em}) at 505 nm when excited at a wavelength of 365 nm. The temperature-dependent photoluminescence spectra, recorded at an excitation wavelength of 365 nm, showed a red shift with the emission maxima from 576 to 584 nm at an increasing temperature range of 80 to 300 K (Figure 6).[38] The

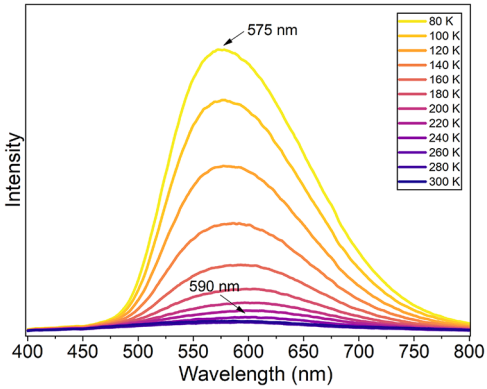

Figure 6. Temperature-dependent photoluminescence (PL) spectra of $[((Cy\text{-}cAI)P(Dipp))_4Ag_4]$ (**2**) in the solid state at 365 nm of excitation wavelength.

photoluminescence quantum yield (Φ_{PL}) of **2** in the solid state was found to be 1.05% with an average lifetime of 3.14 ns (λ_{em} = 505 nm), when excited at a wavelength of 375 nm, indicating a fluorescence process.

The morphology, particle size, and composition of cluster **2** were analyzed using field-emission scanning electron microscopy (FE-SEM) at an accelerating voltage of 3 kV (Figure 7a). The SEM image of **2** revealed block-shaped particles, observed across microscopic scales ranging from 100 μm to 500 nm, forming aggregated structures with well-defined sharp edges, particularly evident at the 20 μm scale. The EDAX spectrum of **2**, employed for the semiquantitative determination of the elemental composition of the cluster, confirmed the presence of Ag, P, C, and N with weight percentages of 21, 5.3, 62.8, and 3.1, respectively, which are consistent with the proposed molecular formula of **2**.

The high-resolution TEM (HR-TEM) images of **2** revealed the formation of well-defined, spherical particles with a crystalline nature, exhibiting an average diameter in the range of 2.81−14.42 nm (Figure 7b). These images further displayed distinct lattice fringes with an interplanar spacing of 0.248 nm. The particle size and interplanar distances were determined using ImageJ software.[49]

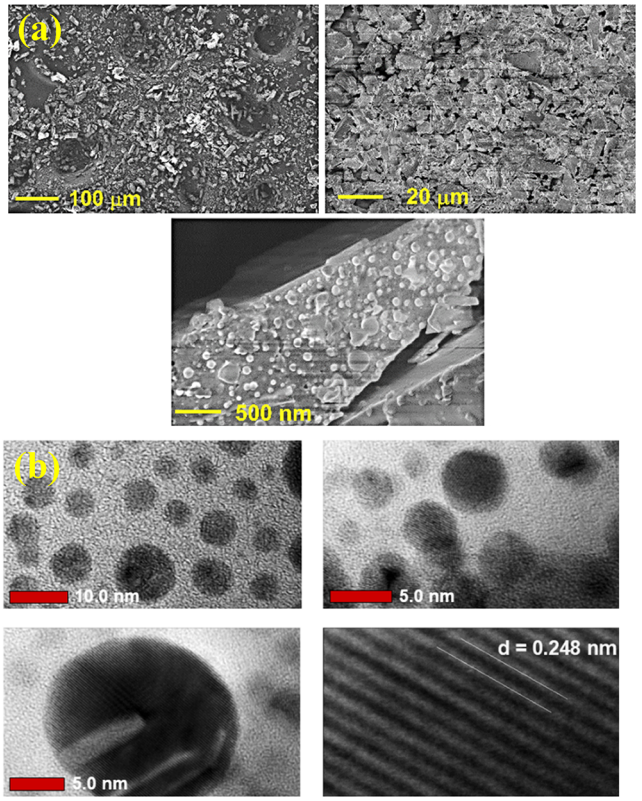

Figure 7. Scanning electron microscopy (SEM) images (a) and high-resolution-TEM images (b) of nanocluster $[(Cy\text{-}cAI)P(Dipp)_4Ag_4]$ (**2**).

To study the adsorption−desorption properties of **2**, BET analysis was carried out, which revealed that **2** possesses a specific surface area of 0.855 m^2g^{-1} and a total pore volume of 0.018 cm^3 g^{-1}, suggesting limited pore availability in the material and an average pore radius of 18.627 Å, which can be considered mesoporous (see SI).[50] The adsorption isotherm showed a Type-II isotherm without the presence of any hysteresis loop, where low nitrogen uptake happens across most of the relative pressure range, with a sharp increase only at higher relative pressures ($P/P_0 > 0.9$), which may be because of capillary condensation in large pores.

On the basis of the initial redox behavior of the present Ag_4 nanocluster **2**, we have attempted to explore the possibility of utilizing this species as an energy storage material. The electrochemical behavior of the Ag_4 electrode, fabricated by depositing the nanocluster **2** on a stainless-steel solid support, was analyzed by employing a three-electrode cell, where the Pt electrode served as the counter electrode and an Ag/AgCl electrode as the reference electrode. On the other hand, the Ag_4 electrode was employed as the working electrode. All electrochemical analyses were done in an aqueous medium with a 1 M $NaClO_4$ electrolyte. Cyclic voltammetry was carried out in the potential range of −0.25 to −1.1 V for determination of the energy storage behavior of the Ag_4 electrode. The electrochemical capacitance and characteristics of the electrode were determined from the CV graphs.[51−53]

The cyclic voltammetry analysis of the Ag_4 electrode was carried out at a range of 2−100 mV s^{-1} over the voltage range of −1.1 to −0.25 V (vs Ag/AgCl). The CV profile demonstrated that the CV curve possesses a quasi-rectangular shape and some deviations with broad humps, revealing the

https://doi.org/10.1021/acs.inorgchem.6c02414
Inorg. Chem. XXXX, XXX, XXX−XXX

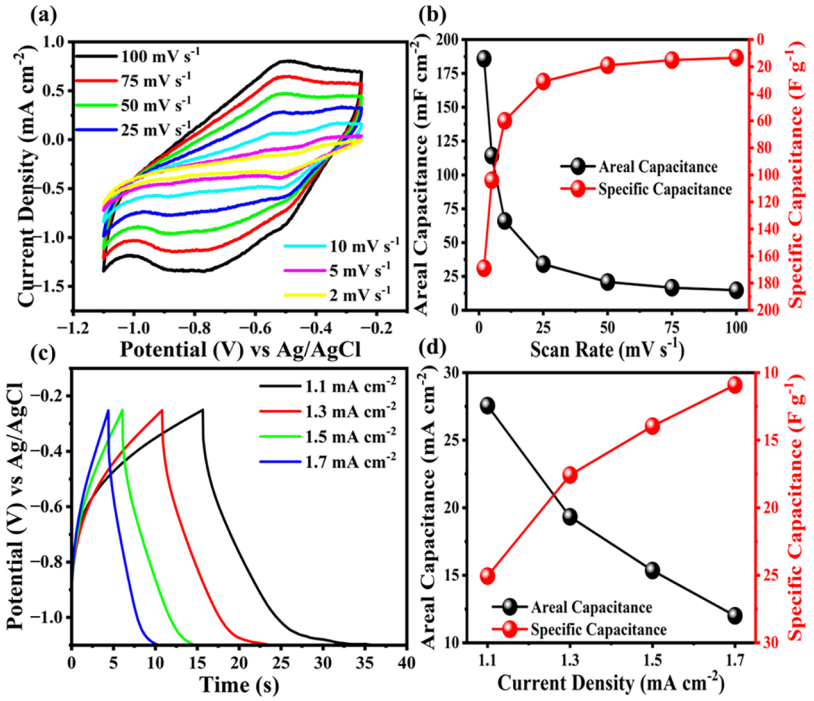

Figure 8. (a) CV plots of Ag_4 electrode, fabricated by depositing nanocluster **2** on a stainless-steel-based solid support at various scan rates. (b) Effect of scan rates on areal and specific capacitance. (c) GCD plots of Ag_4 electrode at different current densities. (d) Effect of current densities on areal and specific capacitance.

simultaneous presence of EDLC as well as pseudocapacitance, as shown in Figure 8a.

A minor anodic peak appeared at approximately −0.4 to −0.5 V and became more pronounced at higher scan rates. Moreover, at higher scan rates, the CV curves exhibited distortion, indicating surface-controlled redox processes, whereas lower scan rates yielded smooth profiles due to good ion diffusion. An increased current density was noted at higher scan rates, but the deformations in the CV curve showed poor availability of ions to the active site of the electrode. As per eqs 1 and 2, the values of areal and specific capacitance for Ag_4 were 185.8 mF cm^{-2} and 168.9 F g^{-1}, respectively, at 2 mV s^{-1}, while both values became 14.7 mF cm^{-2} and 13.4 F g^{-1} at 100 mV s^{-1}, as depicted in Figure 8 (b).

$$\mathrm{Ca} = \frac{\int i\,dV}{A\cdot\Delta V\cdot v} \times 1000 \tag{1}$$

$$\mathrm{Cs} = \frac{\int i\,dV}{m\cdot\Delta V\cdot v} \tag{2}$$

Here, $\int i\,dV$ represents the area under the $C-V$ curve, obtained after integrating current with voltage; A represents the effective surface area of the electrode (cm^2); ΔV represents the voltage range for $C-V$ measurements; v represents the scan rate (mV s^{-1}); and m represents the mass of the material (g).

Further investigations of the electrode's electrochemical characteristics with regard to its usage in supercapacitors were conducted in terms of the galvanostatic charge−discharge (GCD) test through applying different current densities within a certain voltage range. The charge−discharge characteristics of the electrode for three-electrode cells were evaluated considering the equations below, where eq 3 is associated with areal capacitance and eq 4 is associated with specific capacitance.[54−57]

$$\mathrm{Ca} = \frac{I\cdot\Delta t}{A\cdot\Delta V} \tag{3}$$

$$\mathrm{Cs} = \frac{I\cdot\Delta t}{m\cdot\Delta V} \tag{4}$$

Here, I represents the current flowing through the cell, Δt represents the time during which the cell discharges, A stands for the area of the active electrode (cm^2), m represents the mass of the electroactive material (g), and ΔV is the potential window during the experiment.

The GCD test was conducted on the Ag_4 electrode using different current densities of 1.1 to 1.7 mA cm^{-2} as depicted in Figure 8c. From the GCD data, a quasi-triangular shape was obtained with some deviations from linearity, implying that both EDLC and pseudocapacitance are present, which is due to faradic reactions.[58,59] The charge−discharge cycles have reasonable symmetry, implying electrochemical reversibility, despite the slight IR drop at high current density. Most importantly, from eqs 3 and 4, the maximum areal and specific capacitances achieved are 27.5 mF cm^{-2} and 25 F g^{-1} at a current density of 1.1 mA cm^{-2}. With the increase in current density to 1.7 mA cm^{-2}, the areal and specific capacitances decrease to 12 mF cm^{-2} and 10.9 F g^{-1}, as seen in Figure 8d. The reduction in capacitance is because of poor ion diffusion and low active site utilization at high current densities.[60]

In order to study the conductivity and resistance characteristics of the electrode material, EIS experiments were conducted on the three-electrode system within the frequency range of 0.1 Hz to 1 mHz. For this purpose, the data obtained by EIS were analyzed through the use of Nyquist plots. The high-frequency intercept on the real axis signifies the solution resistance (R_s), which is the resistance between the current collector and the electrolyte.[61,62] The small semicircle observed on the high- to midfrequencies relates to the charge transfer

https://doi.org/10.1021/acs.inorgchem.6c02414
Inorg. Chem. XXXX, XXX, XXX−XXX

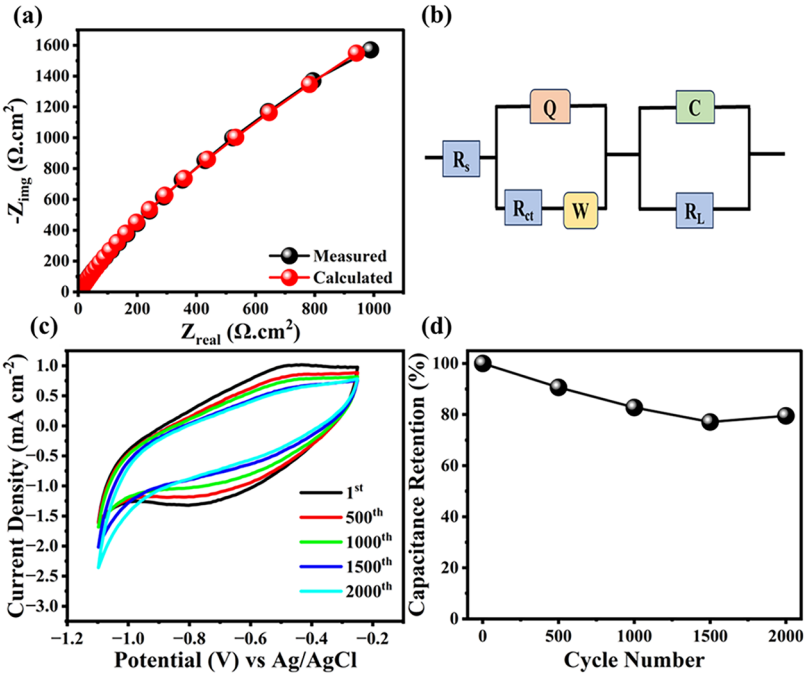

Figure 9. (a) Nyquist plot of Ag_4 electrode measured by the EIS method. (b) Equivalent electrical circuit employed in the fitting process of Nyquist data. (c) *C*−*V* traces recorded for various cycle numbers ranging from 500 to 2000 cycles. (d) Capacitance retention as a function of cycle numbers up to 2000 cycles.

resistance (R_{ct}),[63,64] resulting from the reversible faradaic reactions during the charge−discharge cycle, whereas the inclined straight line in the low-frequency region represents ion diffusion behavior, corresponding to the Warburg impedance. Fitting of the EIS data was done through ZSimpWin, and the optimized equivalent circuit diagram was found to be $R(Q(RW))(CR)$ as presented in Figure 9b. Here, "R_s" refers to solution resistance, "Q" represents a constant phase element due to the nonideality of the capacitor, "R_{ct}" is charge transfer resistance, and "W" denotes ion diffusion. Based on the figure above, it can be seen that Ag_4 shows low solution resistance (R_s = 2.9 Ω), indicating high ionic conductivity, in addition to a low R_{ct} value of 0.76 Ω as evidenced in Figure 9a.

The electrochemical stability of the Ag_4 electrode was further characterized through CV. As indicated by the CV profiles recorded with increasing cycle numbers, there was a steady reduction in the area under the curve, implying the loss of capacitance with increased cycling time, as observed in Figure 9c. The Ag_4 electrode was able to retain about 80% of its initial capacitance value after 2000 cycles, as can be seen in Figure 9d, reflecting modest electrochemical stability. The loss in capacitance may be related to electrode degradation or loss of active sites due to continuous redox reactions. It is noteworthy to mention that Liu et al.[65] prepared an Ag nanoparticle/conductive porous $La_{0.7}Sr_{0.3}CoO_{3-}\delta$ (Ag/LSC) binder-free electrode with a capacitance of 14.8 F cm^{-2} (517.5 F g^{-1}) for 85.6% stability within 3000 cycles. Ansari et al.[66] designed a ternary composite material of Ag-rGO@MnO_2 that showed a high specific capacitance of ∼675 F g^{-1} with ∼95% retention rate over 3000 cycles, due to the combined effect of Ag, rGO, and MnO_2. Also, Kalambate et al.[67] fabricated a ternary GNS/AgNPs/PPY composite that gives ∼450 F g^{-1} with ∼92% stability, where GNS played the role of EDLC behavior, PPY adds pseudocapacitance, and Ag acts as a conductivity enhancer and improves charge transfer rate. Similarly, Patil et al.[68] demonstrated Ag-doped PEDOT:PSS electrodes that show a capacitance of ∼172 F g^{-1} and energy density of ∼36.1 Wh kg^{-1} because of the enhanced redox activity and better electrical conductivity through silver doping. Additionally, the study of Wu et al.[69] designed a 3D high-nucleus Ag_{14} nanopolycluster with an electrode showing 412 F g^{-1} at 1.5 A g^{-1} with ∼94% retention rate over 7000 cycles and energy density of ∼57.2 Wh kg^{-1}, where porous architecture and strong interaction of Ag−S played important roles in enhanced ion diffusivity and stability. However, no reports have been documented featuring a soluble, structurally well-defined molecular Ag_4-based nanocluster, exhibiting pseudocapacitance as a novel energy storage material.

Unlike other Ag-based supercapacitor electrodes that have been extensively studied, the current Ag_4 nanocluster-based electrode represents an entirely new approach to the design of electrochemical capacitors with superior performance at the molecular level. The uniqueness of the Ag_4 nanocluster (**2**) is based on the fact that it possesses a well-defined atomic composition in which charge storage occurs exclusively via redox-active centers of the molecule. This allows for gaining insight into intrinsic EDLC−pseudocapacitive mechanisms of charge storage through the appearance of the quasi-rectangular *C*−*V* curve and characteristic redox peaks. Unlike traditional composite materials, the soluble Ag_4 nanocluster (**2**) functions as a molecular pseudocapacitor, allowing for gaining insight into nanoscale mechanisms of charge storage without any influence of extraneous conductive supports. While the specific capacitance (∼168.9 F g^{-1}) and cycling stability (∼80% after 2000 cycles) are relatively low, the lack of any conductive additives underscores the intrinsic electrochemical activity and structural functionality of the compound.

https://doi.org/10.1021/acs.inorgchem.6c02414
Inorg. Chem. XXXX, XXX, XXX−XXX

CONCLUSIONS

In summary, we have successfully developed a facile synthetic route for the gram-scale synthesis and solid-state isolation of an atomically precise neutral redox-active tetranuclear Ag^I nanocluster (**2**), stabilized by bridging phosphide ligands, which is the first ever phosphide-supported molecular cluster displaying obvious supercapacitive behavior due to the synergistic effect of EDLC and pseudocapacitance with a specific capacitance value of 168.9 F g^{-1} and low internal resistance, suggesting the presence of excellent ionic conductivity and charge transfer performance. Nonetheless, the Ag_4-deposited electrodes presented a reasonable cycle stability of around 80% at 2000 cycles. The absence of conductive additives proved that the charge storage was attributed to intrinsically active redox sites. This study paves the way for exploring molecular cluster-based supercapacitors, where the performance of the materials can be fine-tuned by adjusting the nuclearity, electronic configuration, and specific ligand coordination.

EXPERIMENTAL SECTION

Materials and Methods

All synthetic manipulations were performed using either standard Schlenk line techniques under an argon atmosphere or in an argon-filled MBraun Eco-Plus glovebox, where O_2 and H_2O levels were always kept below 0.1 ppm. All glassware was oven-dried (150 °C) prior to use. Solvents obtained from an MBraun Solvent Purification System (SPS) were further dried by standard methods of refluxing with Na/K alloy for 2 days, followed by vacuum distillation over 4 Å molecular sieves under argon.

Single-Crystal X-ray Diffraction

The single-crystal X-ray data were collected on a Bruker D8 VENTURE diffractometer equipped with a PHOTON III C28 detector using IμS 3.0 microfocus sealed X-ray source with Molybdenum Kα radiation. A complete data set was collected following the strategies generated using the APEX4[70] module of the Bruker software suite. The data reduction was carried out using SAINTPLUS,[71] and multiscan absorption correction was performed using the program SADABS.[71] The crystal structures were solved by the intrinsic phasing method (SHELXT)[71] and were refined with full-matrix least-squares on F_2 using the ShelXle[72] plug-in included in APEX 4. All nonhydrogen atoms were refined anisotropically. OLEX2 Version 1.3.0 was used for structure solution and refinement.[73]

Computational Details

The geometry optimization of cluster **2** was performed using the B3LYP[41a−c] hybrid functional with the dispersion correction term D3(BJ) and Def2-TZVP basis set, in the singlet electronic state, using the Gaussian 09[74] package in the gaseous phase with the help of DFT. The geometry optimization is favored by minima on the potential energy surface, followed by no negative frequency. The NBO 6.0 program[42a−c] is used to perform the NBO calculations of the complexes along with the MEP plot and AIMAll package for QTAIM[45a−d] analysis, both at the B3LYP-D3(BJ)/Def2-TZVP level of theory using the optimized coordinates. To further assess the extent of electron delocalization, electron localization function (ELF)[46] calculations were carried out using the Multiwfn[47a,b] program.

Synthesis of 2

In an oven-dried Schlenk flask, orange crystals of $[((Cy\text{-}cAI)P(Dipp))Cs]_n$**1**, 50 mg, 0.1022 mmol, 1 equiv) and anhydrous $AgNTf_2$ (39.61 mg, 0.1022 mmol, 1 equiv) were weighed in. To this freshly distilled THF was added at rt to obtain a dark greenish solution, which was stirred overnight, resulting in the formation of a greenish-brown reaction solution, which was filtered, concentrated, and stored at a −40 °C freezer from which block-shaped yellow crystals of $[((Cy\text{-}cAI)P(Dipp))_4Ag_4]$ (**2**), suitable for X-ray single-crystal diffraction, were obtained after 2 weeks in 58% yield (55 mg). **^{1}H NMR** (400 MHz, 298 K, THF-d_8) δ: 7.17 (t, J = 8 Hz, 4H), 7.08 (t, J = 8 Hz, 8H), 4.42 (br, 4H), 3.92 (br, 2H), 3.35 (d, J = 8 Hz, 2H), 2.27 (s, 4H), 2.04 (t, J = 8 Hz, 6H), 1.42−1.35 (m, 16H), 1.25 (s, 16H), 1.15 (br, 30H), 1.10 (s, 18H), 1.02 (d, J = 8 Hz, 18H), 0.85 (s, 12H) ppm; **^{13}C {^{1}H} NMR** (101 MHz, 224 K, THF-d_8) δ: 155.2, 134.9, 129.9, 129.0, 124.3, 124.2, 122.7, 119.5, 68.1, 55.5, 52.7, 48.5, 39.9, 39.6, 36.5, 35.1, 32.7, 31.9, 29.0, 26.5, 26.0, 24.6, 24.4, 23.8, 15.8, 14.5 ppm; **^{31}P {^{1}H} NMR** (162 MHz, 223 K, THF-d_8) δ: −109.8 (br m) ppm. **Decomposition point:** 137−140 °C.

Electrode Design

The fabrication of the electrodes, made of Ag_4 nanocluster **2**, was accomplished by utilizing the easy doctor blade technique on a mirror-like polished stainless-steel (SS) substrate. For preparing the electrode slurry, 80 wt % of Ag_4, 10 wt % of PVDF, and 10 wt % of carbon black were mixed in NMP to obtain the electrode slurry with a homogeneous distribution of particles. This mixture was deposited evenly onto the SS substrate via an applicator and then left for drying at 80 °C overnight to ensure good attachment and complete evaporation of the solvent. The mass loading of the active material was estimated from the difference in weight before and after depositing onto the substrate, which resulted in a mass loading of approximately 1.1 mg cm^{-2} for a 1 × 1 cm active electrode area (SS, 46-gauge).

ASSOCIATED CONTENT

Supporting Information

The Supporting Information is available free of charge at https://pubs.acs.org/doi/10.1021/acs.inorgchem.6c02414.

Synthesis, NMR, ESI-MS, FT-IR, UV−vis, fluorescence, XPS, EPR data, detailed quantum chemical calculations, and crystal structure refinement tables (PDF). CCDC 2529079 (**2**) contains the supplementary crystallographic data for this paper. These data can be obtained free of charge from Cambridge Crystallographic Data Centre on application to CCDC. [E-mail: deposit@ccdc.cam.ac.uk] (PDF)

Accession Codes

Deposition Number 2529079 contains the supplementary crystallographic data for this paper. These data can be obtained free of charge via the joint Cambridge Crystallographic Data Centre (CCDC) and Fachinformationszentrum Karlsruhe Access Structures service.

AUTHOR INFORMATION

Corresponding Authors

Sudipta Roy − *Department of Chemistry, Indian Institute of Science Education and Research (IISER) Tirupati, Tirupati, Andhra Pradesh 517619, India;* orcid.org/0000-0002-5883-4329; Email: roy.sudipta@iisertirupati.ac.in

Babasaheb R. Sankapal − *Nanomaterial and Device Laboratory, Department of Physics, Visvesvaraya National Institute of Technology, Nagpur, Maharashtra 440010, India;* orcid.org/0000-0002-7464-9633; Email: brsankapal@phy.vnit.ac.in

Authors

Nivedya K. Vikas − *Department of Chemistry, Indian Institute of Science Education and Research (IISER) Tirupati, Tirupati, Andhra Pradesh 517619, India*

Mayur Thosare − *Nanomaterial and Device Laboratory, Department of Physics, Visvesvaraya National Institute of Technology, Nagpur, Maharashtra 440010, India*

https://doi.org/10.1021/acs.inorgchem.6c02414
Inorg. Chem. XXXX, XXX, XXX−XXX

Sayed Imroz Hossain − *Department of Chemistry, Indian Institute of Science Education and Research (IISER) Tirupati, Tirupati, Andhra Pradesh 517619, India;* orcid.org/0009-0001-9154-7102

Akshara Purushothaman − *Department of Chemistry, Indian Institute of Science Education and Research (IISER) Tirupati, Tirupati, Andhra Pradesh 517619, India*

Asutosh Patra − *Department of Chemistry, Indian Institute of Science Education and Research (IISER) Tirupati, Tirupati, Andhra Pradesh 517619, India;* orcid.org/0000-0002-8570-3121

Ashwath Kudlu − *Department of Chemistry, Indian Institute of Science Education and Research (IISER) Tirupati, Tirupati, Andhra Pradesh 517619, India;* orcid.org/0000-0002-6740-9607

Manasi Baccha − *Nanomaterial and Device Laboratory, Department of Physics, Visvesvaraya National Institute of Technology, Nagpur, Maharashtra 440010, India*

Complete contact information is available at: https://pubs.acs.org/10.1021/acs.inorgchem.6c02414

Notes

The authors declare no competing financial interest.

■ ACKNOWLEDGMENTS

S.R. gratefully acknowledges STARS-IISC, MoE (MoE-STARS/STARS-2/2023-0666), IISER Tirupati, and the central HPC for generous financial support and experimental and computational research facilities. B.R.S. thanks ANRF (CRG/2023/001184).

■ REFERENCES

(1) Simon, P.; Gogotsi, Y. Materials for Electrochemical Capacitors. *Nat. Mater.* **2008**, *7* (11), 845−854.

(2) Shen, J.; Yang, C.; Li, X.; Wang, G. High-Performance Asymmetric Supercapacitor Based on Nano-architectured Polyaniline/Graphene/Carbon Nanotube and Activated Graphene Electrodes. *ACS Appl. Mater. Interfaces* **2013**, *5* (17), 8467−8476.

(3) You, B.; Wang, L.; Li, N.; Zheng, C. Improving the Energy Storage Performance of Graphene through Insertion of Pristine CNTs and Ordered Mesoporous Carbon Coating. *ChemElectroChem* **2014**, *1* (4), 772−778.

(4) Wu, Z.; Xie, J.; Xu, Z. J.; Zhang, S.; Zhang, Q. Recent Progress in Metal−Organic Polymers as Promising Electrodes for Lithium/Sodium Rechargeable Batteries. *J. Mater. Chem. A* **2019**, *7* (9), 4259−4290.

(5) Liu, C.; Li, F.; Ma, L.; Cheng, H. Advanced Materials for Energy Storage. *Adv. Mater.* **2010**, *22* (8), E28−E62.

(6) Wang, G.; Zhang, L.; Zhang, J. A Review of Electrode Materials for Electrochemical Supercapacitors. *Chem. Soc. Rev.* **2012**, *41* (2), 797−828.

(7) Jiang, J.; Li, Y.; Liu, J.; Huang, X.; Yuan, C.; Xiong, L. Recent Advances in Metal Oxide-based Electrode Architecture Design for Electrochemical Energy Storage. *Adv. Mater.* **2012**, *24* (38), 5166−5180.

(8) Devan, R. S.; Patil, R. A.; Lin, J.; Ma, Y. One-Dimensional Metal-Oxide Nanostructures: Recent Developments in Synthesis, Characterization, and Applications. *Adv. Funct. Mater.* **2012**, *22* (16), 3326−3370.

(9) Mahmood, N.; Tahir, M.; Mahmood, A.; Zhu, J.; Cao, C.; Hou, Y. Chlorine-doped Carbonated Cobalt Hydroxide for Supercapacitors with Enormously High Pseudocapacitive Performance and Energy Density. *Nano Energy* **2015**, *11*, 267−276.

(10) Zhang, F.; Xiao, F.; Dong, Z. H.; Shi, W. Synthesis of Polypyrrole Wrapped Graphene Hydrogels Composites as Supercapacitor Electrodes. *Electrochim. Acta* **2013**, *114*, 125−132.

(11) Fan, L.-Q.; Liu, G.; Wu, J.; Liu, L.; Lin, J.; Wei, Y. Asymmetric Supercapacitor Based on Graphene Oxide/Polypyrrole Composite and Activated Carbon Electrodes. *Electrochim. Acta* **2014**, *137*, 26−33.

(12) Dai, Y.; Tang, S.; Vongehr, S.; Meng, X. Silver NanoparticleInduced Growth of NanowireCovered Porous MnO_2 Spheres with Superior Supercapacitance. *ACS Sustainable Chem. Eng.* **2014**, *2* (4), 692−698.

(13) Sawangphruk, M.; Suksomboon, M.; Kongsupornsak, K.; Khuntilo, J.; Srimuk, P.; Sanguansak, Y.; Klunbud, P.; Suktha, P.; Chiochan, P. Highperformance Supercapacitors Based on Silver Nanoparticle−Polyaniline−Graphene Nanocomposites Coated on Flexible Carbon Fiber Paper. *J. Mater. Chem. A* **2013**, *1* (34), 9630−9636.

(14) Peng, S.; Li, L.; Tan, H.; Wu, Y.; Cai, R.; Yu, H.; Huang, X.; Zhu, P.; Ramakrishna, S.; Srinivasan, M.; Yan, Q. Monodispersed Ag Nanoparticles Loaded on the PVPassisted Synthetic $Bi_2O_2CO_3$ Microspheres with Enhanced Photocatalytic and Supercapacitive Performances. *J. Mater. Chem. A* **2013**, *1* (26), 7630−7638.

(15) Zhang, L.; Ji, X.; Si, H.; Zhang, Y.; Sha, L.; Chen, H.; Zhao, X. High-performance Supercapacitor Poplar Catkin Ag/Carbon Fibers Composites. *Appl. Phys. A:Mater. Sci. Process.* **2020**, *126* (10), No. 803.

(16) Frackowiak, E.; Khomenko, V.; Jurewicz, K.; Lota, K.; Béguin, F. Supercapacitors Based on Conducting Polymers/Nanotubes Composites. *J. Power Sources* **2006**, *153* (2), 413−418.

(17) Shen, C.-H.; Chuang, C.; Gu, Y.; Ho, W. H.; Song, Y.; Chen, Y.; Wang, Y.; Kung, C. Cerium-Based Metal−Organic Framework Nanocrystals Interconnected by Carbon Nanotubes for Boosting Electrochemical Capacitor Performance. *ACS Appl. Mater. Interfaces* **2021**, *13* (14), 16418−16426.

(18) Hao, X.; Zhang, S.; Xu, Y.; Tang, L.; Inoue, K.; Saito, M.; Ma, S.; Chen, C.; Xu, B.; Adschiri, T.; Ikuhara, Y. Surfactantmediated Morphology Evolution and Selfassembly of Cerium Oxide Nanocrystals for Catalytic and Supercapacitor Applications. *Nanoscale* **2021**, *13* (23), 10393−10401.

(19) (a) Yam, V. W.; Au, V. K.; Leung, S. Y. Light-Emitting Self-Assembled Materials Based on d_8 and d_{10} Transition Metal Complexes. *Chem. Rev.* **2015**, *115* (15), 7589−7728. (b) Du, Y.; Sheng, H.; Astruc, D.; Zhu, M. Atomically Precise Noble Metal Nanoclusters as Efficient Catalysts: A Bridge between Structure and Properties. *Chem. Rev.* **2020**, *120* (2), 526−622.

(20) (a) Sculfort, S.; Braunstein, P. Intramolecular d_{10}−d_{10} Interactions in Heterometallic Clusters of the Transition Metals. *Chem. Soc. Rev.* **2011**, *40* (5), 2741−2760. (b) Schmidbaur, H.; Schier, A. Aurophilic Interactions as a Subject of Current Research: An Up-Date. *Chem. Soc. Rev.* **2012**, *41* (1), 370−412. (c) Schmidbaur, H.; Schier, A. Argentophilic Interactions. *Angew. Chem., Int. Ed.* **2015**, *54* (3), 746−784.

(21) (a) Njogu, E. M.; Omondi, B.; Nyamori, V. O. Review: Multimetallic Silver(I)−Pyridinyl Complexes: Coordination of Silver-(I) and Luminescence. *J. Coord. Chem.* **2015**, *68* (19), 3389−3431. (b) Wang, Q.-M. Thomas. Argentophilicity and Solvent-Induced Structural Diversity in Double Salts of Silver Acetylide with Silver Perfluoroalkyl Carboxylates. *J. Am. Chem. Soc.* **2001**, *123* (31), 7594−7600. (c) Liao, J.-H.; Latouche, C.; Li, B.; Kahlal, S.; Saillard, J.-Y.; Liu, C. W. A Twelve-Coordinated Iodide in a Cuboctahedral Silver(I) Skeleton. *Inorg. Chem.* **2014**, *53* (4), 2260−2267. (d) Dhayal, R. S.; Liao, J.; Liu, Y.; Chiang, M.; Kahlal, S.; Saillard, J.; W, L. C. $[Ag_{21}\{S_2P(O^iPr)_2\}_{12}]^+$: An Eight-Electron Superatom. *Angew. Chem., Int. Ed.* **2015**, *54* (12), 3702−3706. (e) Dhayal, R. S.; Lin, Y.; Liao, J.; Chen, Y.; Liu, Y.; Chiang, M.; Kahlal, S.; Saillard, J.; Liu, C. W. $[Ag_{20}\{S_2P(OR)_2\}_{12}]$: A Superatom Complex with a Chiral Metallic Core and High Potential for Isomerism. *Chem. - Eur. J.* **2016**, *22* (29), 9943−9947. (f) Wang, Q.-M.; Lin, Y.-M.; Liu, K.-G. Role of Anions Associated with the Formation and Properties of Silver Clusters. *Acc. Chem. Res.* **2015**, *48* (6), 1570−1579. (g) Scheer, M.; Gregoriades, L.

J.; Virovets, A. V.; Kunz, W.; Neueder, R.; Krossing, I. Reversible Formation of Polymeric Chains by Coordination of Pentaphosphaferrocene with Silver(I) Cations. *Angew. Chem., Int. Ed.* **2006**, *45* (34), 5689−5693.
(22) Gupta, R. K.; Wang, Z.; Mohan, B.; Tung, C.; Sun, D. Advancements in Atomically Precise Nanocluster Protected by Thiacalix[4]Arene. *Adv. Mater.* **2024**, *36* (45), No. 2410054.
(23) Liu, Z.-Y.; Nie, Q.; Han, B.; Gupta, R. K.; Dong, G.; Luo, G.; Yang, Z.; Sun, D. Atom-precise Coinage Metal Nanoclusters for Nearinfrared Emission: Excited-state Dynamics and Mechanisms. *Chem. Soc. Rev.* **2025**, *54* (19), 9092−9115.
(24) Gupta, R. K.; Mohan, B.; Wang, Z.; Yang, Y.; Sun, D. Atomically Precise Metal Nanoclusters: Emerging Materials for Near-Infrared II Photoluminescence. *Acc. Chem. Res.* **2026**, *59* (3), 476−486.
(25) Xue, J.; Xu, J.; Ren, J.; Liang, Q.; Ou, Q.; Wang, R.; Shuai, Z.; Qiao, J. Intermolecular Charge-transfer Aggregates Enable High-efficiency Near-infrared Emissions by Nonadiabatic Coupling Suppression. *Sci. China Chem.* **2021**, *64* (10), 1786−1795.
(26) Xu, T.; Paul, S.; Zhang, C.; Azam, M.; Han, B. L.; Si, W. D.; Wang, Z.; Gao, Z. Y.; Anoop, A.; Tung, C. H.; Sun, D. Boosting Circularly Polarized Luminescent and Decagram-Scale Mechanochemistry Synthesis of Atomically Precise Superstructure from Achiral Silver Cluster and Chiral Cyclodextrin. *CCS Chem.* **2024**, *7* (2), 519−531.
(27) Xu, Y.; Pu, Y.; Zhang, Q.; Kang, X.; Zhu, M. Order-by-order Control over the Nonlinear Optical Properties of Atomically Precise Nanoclusters. *Chin. J. Struct. Chem.* **2025**, *44* (10), No. 100735.
(28) Zhang, C.; Si, W.; Tian, W.; Xiao, W.; Gao, Z.; Wang, Z.; Tung, C.; Sun, D. Single-atom "Surgery" on Chiral All-dialkynyl-protected Superatomic Silver Nanoclusters. *Sci. Bull.* **2025**, *70* (3), 365−372.
(29) Liu, K.-G.; Rouhani, F.; Shan, Q.; Wang, R.; Li, J.; Hu, M.; Cheng, X.; Morsali, A. Ultrasonicassisted Fabrication of Thinfilm Electrochemical Detector of H_2O_2 Based on Ferrocenefunctionalized Silver Cluster. *Ultrason. Sonochem.* **2019**, *56*, 305−312.
(30) Artem'ev, A. V.; Bagryanskaya, I. Y.; Doronina, E. P.; Tolstoy, P. M.; Gushchin, A. L.; Rakhmanova, M. I.; Ivanov, A. Y.; Suturina, A. O. A New Family of Clusters Containing a Silver-Centered Tetracapped $[Ag@Ag_4(\mu_3\text{-}P)_4]$ Tetrahedron, Inscribed within a N_{12} Icosahedron. *Dalton Trans.* **2017**, *46* (37), 12425−12429.
(31) Nag, E.; Francis, M.; Putta, D.; Roy, S. Isolation of (Aryl)-(Imino)Phosphide and (Aryl)-(Phosphaalkene) Amide Complexes of Alkali Metals from Carbene-Phosphinidenes under Reductive-Thermal Rearrangements. *Chem. - Eur. J.* **2023**, *29* (65), No. e202303433.
(32) Stoll, S.; Schweiger, A. EasySpin, a Comprehensive Software Package for Spectral Simulation and Analysis in EPR. *J. Magn. Reson.* **2006**, *178* (1), 42−55.
(33) Pavlidis, S.; Teutloff, C.; Buzanich, A. G.; Krause, K. B.; Emmerling, F.; Bittl, R.; Abbenseth, J. A Crystalline Bismuth(II) Radical Anion: Synthesis, Characterization, and Reactivity. *Angew. Chem., Int. Ed.* **2025**, *64* (49), No. e202515545.
(34) Nag, E.; Patra, A.; Francis, M.; Patra, U.; Roy, S. Monoanionic Phosphorus-Supported Air Stable $Cu(I)_8$, $Ag(I)_7$, and $Ag(I)_5$ Nanoclusters Exhibiting TADF: A Novel Photocatalyst for Stereoselective Carbene Transfer Reactions. *Adv. Optical Mater.* **2024**, *12* (9), No. 2301256.
(35) Nag, E.; Battuluri, S.; Chandra Mondal, K.; Roy, S. Isolation of Homo-/Mixed-Valence Ag_{12}, Ag_{29}, and Ag_8 Clusters Stabilized by Cyclic Alkyl(Amino) Carbene-Anchored Monoanionic Phosphorus Ligand. *Chem. - Eur. J.* **2022**, *28* (64), No. e202203378.
(36) Edwards, H. G. M.; Farwell, D. W. The Vibrational Spectrum of Trimethylphosphine-Silver Iodide, $[AgI{\cdot}P(CH_3)_3]_4$. *J. Mol. Struct.* **1989**, *197*, 203−212.
(37) Goel, R. G.; Pilon, P. Tri-Tert-Butylphosphine Complexes of Silver(I). Preparation, Characterization, and Spectral Studies. *Inorg. Chem.* **1978**, *17* (10), 2876−2879.
(38) Ishii, R.; Wada, Y.; Sunada, Y. Silyl and Germyl-bridged Neutral Square-planar Ag_4 Clusters with Short Ag−Ag Distances Exhibiting Red Emission. *Chem. Commun.* **2025**, *61* (22), 4391−4394.
(39) Wang, Z.; Wang, Y.; Zhang, C.; Zhu, Y.; Song, K.; Aikens, C. M.; Tung, C.; Sun, D. Silvery Fullerene in Ag_{102} Nanosaucer. *Natl. Sci. Rev.* **2024**, *11* (7), No. nwae192.
(40) Francis, M.; Patra, A.; Salam, F. A.; Prathapa, S. J.; Roy, S. Isolation of Mixed Valence Charge-Neutral Ag_{12}, and Dicationic Ag_{10} Nano-Clusters Stabilized by Carbene-Phosphaalkenides. *Chem. Commun.* **2025**, *61* (7), 1379−1382.
(41) (a) Becke, A. D. Density-Functional Exchange-Energy Approximation with Correct Asymptotic Behavior. *Phys. Rev. A* **1988**, *38* (6), 3098−3100. (b) Perdew, J. P. Density-Functional Approximation for the Correlation Energy of the Inhomogeneous Electron Gas. *Phys. Rev. B* **1986**, *33* (12), 8822−8824. (c) Weigend, F.; Ahlrichs, R. Balanced Basis Sets of Split Valence, Triple Zeta Valence and Quadruple Zeta Valence Quality for H to Rn: Design and Assessment of Accuracy. *Phys. Chem. Chem. Phys.* **2005**, *7* (18), 3297−3305.
(42) (a) Reed, A. E.; Weinstock, R. B.; Weinhold, F. Natural Population Analysis. *J. Chem. Phys.* **1985**, *83*, 735−746. (b) Reed, A. E.; Curtiss, L. A.; Weinhold, F. Intermolecular Interactions from a Natural Bond Orbital, Donor-Acceptor Viewpoint. *Chem. Rev.* **1988**, *88*, 899−926. (c) Glendening, E. D.; Landis, C. R.; Weinhold, F. NBO 6.0: Natural Bond Orbital Analysis Program. *J. Comput. Chem.* **2013**, *34* (16), 1429−1437.
(43) Wiberg, K. B. Application of the Pople-Santry-Segal CNDO Method to the Cyclopropylcarbinyl and Cyclobutyl Cation and to Bicyclobutane. *Tetrahedron* **1968**, *24* (3), 1083−1096.
(44) Stevenson, J.; Sorenson, B.; Subramaniam, V. H.; Raiford, J.; Khlyabich, P. P.; Loo, Y.-L.; Clancy, P. Mayer Bond Order as a Metric of Complexation Effectiveness in Lead Halide Perovskite Solutions. *Chem. Mater.* **2017**, *29*, 2435−2444.
(45) (a) Bader, R. F. W. A quantum theory of molecular structure and its applications. *Chem. Rev.* **1991**, *91*, 893−928. (b) Bader, R. F. W. *Atoms in Molecules: A Quantum Theory*; Clarendon Press: Oxford, 1990. (c) Bader, R. F. W. Atoms in Molecules. *Acc. Chem. Res.* **1985**, *18*, 9−15. (d) Matta, C. F.; Boyd, R. J. *The Quantum Theory of Atoms in Molecules: From Solid State to DNA and Drug Design*; Wiley-VCH: Weinheim, 2007.
(46) Tian, L.; Fei-Wu, C. Meaning and Functional Form of the Electron Localization Function. *Acta Phys-chim Sin.* **2011**, *27*, 2786−2792.
(47) (a) Lu, T.; Chen, F. Multiwfn: A Multifunctional Wavefunction Analyzer. *J. Comput. Chem.* **2012**, *33*, 580−592. (b) Lu, T. A. *J. Chem. Phys.* **2024**, *161*, 082503−082541.
(48) (a) Miertuš, S.; Scrocco, E.; Tomasi, J. Electrostatic Interaction of a Solute with a Continuum. A Direct Utilizaion of AB Initio Molecular Potentials for the Prevision of Solvent Effects. *J. Chem. Phys.* **1981**, *55*, 117−129. (b) Tomasi, J.; Mennucci, B.; Cammi, R. Quantum Mechanical Continuum Solvation Models. *Chem. Rev.* **2005**, *105*, 2999−3094.
(49) Schneider, C. A.; Rasband, W. S.; Eliceiri, K. W. NIH Image to ImageJ: 25 Years of Image Analysis. *Nat. Methods* **2012**, *9* (7), 671−675.
(50) Horikawa, T.; Do, D. D.; Nicholson, D. Capillary condensation of adsorbates in porous materials. *Adv. Colloid Interface Sci.* **2011**, *169* (1), 40−58.
(51) Das, S.; Thosare, M.; Ghosh, S.; Shivasharma, T. K.; Ahamed, S.; Karnamkkott, H. S.; Schwarz, B.; Sankapal, B. R.; Ungur, L.; Chandra Mondal, K. Air Stable Photo-Redox Active Elusive Cr(III)-Tri-Dithiolene-Radical Complexes as a New Class of Pseudo-Supercapacitors with High Capacitance: Enhancement of Energy Storage with Heavier Chalcogenide. *J. Mater. Chem. A* **2026**, *14*, 10178−10198.
(52) Thosare, M.; Deshmukh, T. B.; Bulakhe, R. N.; Kim, J. M.; Sankapal, B. R. Graphitic Carbon Nitride: A Comprehensive Review towards Supercapacitive Energy Storage Applications. *J. Energy Storage* **2025**, *130*, No. 117338.

https://doi.org/10.1021/acs.inorgchem.6c02414
Inorg. Chem. XXXX, XXX, XXX−XXX

(53) Parashtekar, A.; Bourgeois, L.; Tatiparti, S. S. V. Stoichiometry−Grain Size-Specific Capacitance Interrelationships in Nickel Oxide. *RSC Adv.* **2022**, *12*, 8333−8344.
(54) Shivasharma, T. K.; Sahu, R.; Thosare, M.; Sarker, D.; Deshpande, U.; Sankapal, B. R. Device Grade Solid-State Pouch and Coin Cell Supercapacitors Dual Assembly Using Consumed Battery Waste to Best Utilization. *Sci. Rep.* **2025**, *15*, No. 28406.
(55) Mondal, S.; Kedara, S. T.; Das, S.; Thosare, M.; Mascarenhas, C. L.; Sankapal; Babasaheb, R.; Mondal, C. Novel Redox-active Vanadium(V) Dithiolene Complexes for Efficient Supercapacitive Energy Storage: Role of Selenium Functionalization on Pseudocapacitive Properties. *J. Mater. Chem. A* **2026**, *14*, 14923−14939.
(56) Deshmukh, T. B.; Pande, S.; Thosare, M.; Agarwal, A.; Sankapal, S. R.; Sankapal, B. R. Engraved Rectangular $Ni_3Fe_4(PO_4)_6$ Microrods on MWCNTs: A Promising Electrode Architecture for Scalable Supercapacitive Devices. *Diam. Rel. Mater.* **2026**, *165*, No. 113589.
(57) Sethi, M.; Sandhya, S. U.; Krishna, B. D. A. Porous Graphene−$NiFe_2O_4$ Nanocomposite with High Electrochemical Performance and High Cycling Stability for Energy Storage Applications. *Nanoscale Adv.* **2020**, *2*, 4229−4241.
(58) Gupta, S.; Kujur, P.; Paul, A. Activated Carbon Framework from Carbon Nanospheres as Supercapacitor: Comparative Effects of Acidic, Alkaline, and Neutral Activation. *ChemPhysChem* **2026**, *27*, No. e202500791.
(59) Hatami-Kakesh, S.; Zeinali, S.; Zerafat, M. M. Enhanced Supercapacitor Performance via Synergistic Integration of MOFs and Polyaniline: Structural and Electrochemical Investigations. *Surf. Interfaces* **2025**, *75*, No. 107757.
(60) Zhu, Z.; Liu, Y.; Zhang, H.; Xu, Y.; Shao, Z.; Ge, L.; Wang, Z.; Chen, H. Emerging Trends in Electrochemical Energy Storage: A Focus on Low-temperature Pseudocapacitors. *Energy Rev.* **2025**, *4*, No. 100118.
(61) Civan, F. E.; Zabara, M. A.; Katırcı, G.; Ülgüt, B. Temperature-Dependent Electrochemical Impedance Spectroscopy of Batteries. *ACS Electrochem.* **2026**, *2*, 825−844.
(62) Fukuma, S.; Yoshii, K.; Tabuchi, M.; Uchida, S. Electrochemical Impedance Analysis of the Charge Transfer Mechanism on $Li_4Ti_5O_{12}$ Surface in the Presence or Absence of the Solid/Electrolyte Interface Film. *J. Electroanal. Chem.* **2024**, *971*, No. 118586.
(63) Mc Carthy, K.; Gullapalli, H.; Ryan, K. M.; Kennedy, T. Electrochemical Impedance Correlation Analysis for the Estimation of Li-Ion Battery State of Charge, State of Health and Internal Temperature. *J. Energy Storage* **2022**, *50*, No. 104608.
(64) Li, T.; Wang, D.; Wang, H. New Method for Acquisition of Impedance Spectra from Charge/Discharge Curves of Lithiumion Batteries. *J. Power Sources* **2022**, *535*, No. 231483.
(65) Liu, P.; Liu, J.; Cheng, S.; Cai, W.; Yu, F.; Zhang, Y.; Wu, P.; Liu, M. A High-performance Electrode for Supercapacitors: Silver Nanoparticles Grown on a Porous Perovskite-type Material $La_{0.7}Sr_{0.3}CoO_{3-\delta}$ Substrate. *Chem. Eng. J.* **2017**, *328*, 1−10.
(66) Ansari, A. R.; Ansari, S. A.; Parveen, N.; Ansari, M. O.; Osman, Z. Silver Nanoparticle Decorated on Reduced Graphene Oxide-Wrapped Manganese Oxide Nanorods as Electrode Materials for High-Performance Electrochemical Devices. *Crystals* **2022**, *12*, No. 389.
(67) Kalambate, P. K.; Dar, R. A.; Karna, S. P.; Srivastava, A. K. Corrigendum to "High Performance Supercapacitor Based on Graphene-Silver Nanoparticles-Polypyrrole Nanocomposite Coated on Glassy Carbon Electrode. *J. Power Sources* **2015**, *278*, 828.
(68) Patil, D. S.; Pawar, S. A.; Hwang, J.; Kim, J. H.; Patil, P. S.; Shin, J. C. Silver Incorporated PEDOT: PSS for Enhanced Electrochemical Performance. *J. Ind. Eng. Chem.* **2016**, *42*, 113−120.
(69) Wu, Q.-S.; Bigdeli, F.; Rouhani, F.; Gao, X.; Kaviani, H.; Li, H.; Wang, W.; Liu, K.; Hu, M.; Cai, X.; Morsali, A. New 3D Porous Silver Nanopolycluster as a Highly Effective Supercapacitor Electrode: Synthesis and Study of the Optical and Electrochemical Properties. *Inorg. Chem.* **2021**, *60*, 1523−1532.
(70) Bruker*APEX4, SAINT and SADABS*; Bruker AXS Inc: Madison, WI, USA, 2021.
(71) M Sheldrick, G. M. Crystal structure refinement with *SHELXL*. *Acta Crystallogr., Sect. C:Struct. Chem.* **2015**, *71* (1), 3−8.
(72) Hübschle, C. B.; Sheldrick, G. M.; Dittrich, B. *ShelXle*: A Qt Graphical User Interface for *SHELXL*. *J. Appl. Crystallogr.* **2011**, *44*, 1281−1284.
(73) Dolomanov, O. V.; Bourhis, L. J.; Gildea, R. J.; Howard, J. A. K.; Puschmann, H. OLEX2: A Complete Structure Solution, Refinement and Analysis Program. *J. Appl. Crystallogr.* **2009**, *42*, 339−341.
(74) Frisch, M. J.; Trucks, G. W.; Schlegel, H. B.; Scuseria, G. E.; Robb, M. A.; Cheeseman, J. R.; Scalmani, G.; Barone, V.; Petersson, G. A.; Nakatsuji, H.; Li, X.; Caricato, M.; Marenich, A.; Bloino, J.; Janesko, B. G.; Gomperts, R.; Mennucci, B.; Hratchian, H. P.; Ortiz, J. V.; Izmaylov, A. F.; Sonnenberg, J. L.; Williams-Young, D.; Ding, F.; Lipparini, F.; Egidi, F.; Goings, J.; Peng, B.; Petrone, A.; Henderson, T.; Ranasinghe, D.; Zakrzewski, V. G.; Gao, J.; Rega, N.; Zheng, G.; Liang, W.; Hada, M.; Ehara, M.; Toyota, K.; Fukuda, R.; Hasegawa, J.; Ishida, M.; Nakajima, T.; Honda, Y.; Kitao, O.; Nakai, H.; Vreven, T.; Throssell, K.; Montgomery, J. A., Jr.; Peralta, J. E.; Ogliaro, F.; Bearpark, M.; Heyd, J. J.; Brothers, E.; Kudin, K. N.; Staroverov, V. N.; Keith, T.; Kobayashi, R.; Normand, J.; Raghavachari, K.; Rendell, A.; Burant, J. C.; Iyengar, S. S.; Tomasi, J.; Cossi, M.; Millam, J. M.; Klene, M.; Adamo, C.; Cammi, R.; Ochterski, J. W.; Martin, R. L.; Morokuma, K.; Farkas, O.; Foresman, J. B.; Fox, D. J. *Gaussian 09*, revision D.01; Gaussian, Inc.: Wallingford, CT, 2016.

https://doi.org/10.1021/acs.inorgchem.6c02414
Inorg. Chem. XXXX, XXX, XXX−XXX